Correction of the IRD Influence for Paleo-Current Flow Speed Reconstructions in Hemipelagic Sediments

N. Stevenard, A. Govin, C. Kissel, A. van Toer

Paleoceanography and Paleoclimatology

AGU ADVANCING EARTH AND SPACE SCIENCE

RESEARCH ARTICLE
10.1029/2022PA004500

Correction of the IRD Influence for Paleo-Current Flow Speed Reconstructions in Hemipelagic Sediments

N. Stevenard[1], A. Govin[1], C. Kissel[1], and A. Van Toer[1]

[1]Laboratoire des Sciences du Climat et de l'Environnement, LSCE/IPSL, CEA-CNRS-UVSQ, Université Paris-Saclay, Gif-sur-Yvette, France

Key Points:

- Evidence for unsorted Ice-Rafted Detritus (IRD) influence on $\overline{SS}$ records of hemipelagic sediments in subpolar environments
- New method proposed to provide grain-size distributions free of unsorted IRD influence
- Allows to define a paleo-current strength proxy free of unsorted IRD contribution

Supporting Information:

Supporting Information may be found in the online version of this article.

Correspondence to:

N. Stevenard,
nathan.stevenard@lsce.ipsl.fr

Citation:

Stevenard, N., Govin, A., Kissel, C., & Van Toer, A. (2023). Correction of the IRD influence for paleo-current flow speed reconstructions in hemipelagic sediments. *Paleoceanography and Paleoclimatology*, *38*, e2022PA004500. https://doi.org/10.1029/2022PA004500

Received 24 JUN 2022
Accepted 30 JAN 2023

Author Contributions:

Conceptualization: N. Stevenard, A. Govin, C. Kissel
Formal analysis: N. Stevenard, A. Govin, A. Van Toer
Funding acquisition: A. Govin
Investigation: N. Stevenard
Methodology: N. Stevenard, A. Govin, C. Kissel, A. Van Toer
Project Administration: A. Govin
Software: N. Stevenard
Supervision: A. Govin, C. Kissel
Writing – original draft: N. Stevenard
Writing – review & editing: N. Stevenard, A. Govin, C. Kissel, A. Van Toer

Abstract Reconstructions of past changes in deep-sea current intensities are needed to understand ocean-climate interactions in the past. The mean size of the sortable silt fraction (10–63 μm, $\overline{SS}$) is one of the most used proxies in this domain. However, in polar and subpolar environments under relatively low flow speed conditions, the presence of Ice-Rafted Detritus (IRD) may alter the $\overline{SS}$ record and thus bias the interpretation of paleo-current strength changes. In this paper, we examine the influence of IRD on the $\overline{SS}$ record of three sedimentary cores from the subpolar North Atlantic and the Antarctic margin. The influence of unsorted IRD on $\overline{SS}$ records is clearly established. To remove this IRD influence on grain-size distributions (GSDs), we propose a new method based on End-Member Analysis approach, and for which a MATLAB script is made available. This method characterizes the GSD of the unsorted IRD input, allowing it to be isolated and discarded, and the current sensitive $\overline{SS}$ variability to be robustly identified. The method therefore allows the recalculation of a modified sediment GSD free of unsorted IRD influence and the construction of modified $\overline{SS}$ and sortable silt percentage (the % of the 10–63 μm in the total <63 μm fraction) records. The application of the method to the three studied cores shows that (a) the unsorted IRD component is correctly removed from the grain-size signal and (b) the new $\overline{SS}$ record is consistent with the XRF-based ln(Zr/Rb) grain-size proxy.

1. Introduction

Changes in the deep oceanic circulation, a major component of the global thermohaline circulation, may have an important impact on the Earth's climate. A proxy of the strength of bottom currents, initially proposed by McCave et al. (1995) and largely used to reconstruct past changes in the deep ocean circulation, is the mean size of sortable silt ($\overline{SS}$), which covers the 10–63 μm range of the non-cohesive silt fraction. Its use as a proxy for bottom-current strength relies on the fact that hydrodynamic processes of sorting in the viscous sublayer tend to act on particles greater than 10 μm (McCave & Hall, 2006). In sedimentary records from polar or subpolar environments, the sediment is in many cases a mixture of material supplied and sorted by bottom currents and of IRD (L. Wu et al., 2020). Because IRD generally cover the entire grain-size spectrum (J. Andrews, 2000; J. T. Andrews & Principato, 2002), they may influence $\overline{SS}$ values. McCave and Andrews (2019) proposed to use the volume (%) of the >250 μm fraction obtained from laser granulometer as an IRD proxy. In the Drake Passage, which is characterized by high bottom-current flow speed, studies suggested an extension of the sortable range up to 125 μm (Lamy et al., 2015; S. Wu et al., 2021). In that case, IRD are thus also represented by medium to coarse sand fractions (e.g., >250 μm). Other studies consider the whole sand content (63 μm–2 mm; Hass, 2002; Hoffmann et al., 2019) as a tracer of IRD. These different size ranges of current-sorted and unsorted particles depend on environments and hydrodynamic conditions. If the limit between current-sorted and vertically advected particles may therefore be shifted toward grain-size >63 μm in environments with high flow speed conditions (S. Wu et al., 2021), this boundary may be shifted toward finer grain-size (<63 μm) in lower hydrodynamical conditions or areas with higher flux of material supplied. In that case, IRD may bias $\overline{SS}$ values (Hass, 2002; Jonkers et al., 2015). Despite these variable limits of grain-size range to trace IRD, the influence of IRD on $\overline{SS}$ values is poorly constrained. On the one hand, McCave and Andrews (2019) suggest that fine (i.e., silt-clay) IRD do not behave differently from any other particles and are current-sorted. On the other hand, other studies (Hass, 2002; Jonkers et al., 2015) consider that the contribution of unsorted IRD on $\overline{SS}$ values should be removed to obtain a true record of past flow speed. For that, various approaches have been proposed.

The degree of correlation between $\overline{SS}$ and the percentage of sortable silt (i.e., the percent of the 10–63 μm in the <63 μm fraction, SS%) is defined as the index of sorting. High values ($r > 0.5$) would support $\overline{SS}$ as paleo-current strength proxy, while low values could result from a significant contribution of IRD, without allowing the possibility of correcting for this IRD influence (McCave & Andrews, 2019; McCave & Hall, 2006; McCave et al., 1995).

An alternative to reconstruct true past current strength variability is the use of $\Delta\overline{SS}$ which is the result of the subtraction of the regression between $\overline{SS}$ (phi scale) and sand (%) from the initial $\overline{SS}$ (Hass, 2002). However, the lack of accuracy in most of the regression calculations makes this method poorly precise (Hoffmann et al., 2019; Li & Piper, 2015). Jonkers et al. (2015) have proposed another method to remove IRD influence using inverse modeling or End-Member-Analyses (EMA). The EMA consists in a statistical decomposition of the grain-size datasets resulting in the determination of "End-Members" (EM) and of their respective contributions to all grain-size spectra (Dietze et al., 2012; Paterson & Heslop, 2015; Seidel & Hlawitschka, 2015; Weltje, 1997; Zhang et al., 2020). In the Jonkers et al. (2015) study, the IRD correction consists of a ratio between the two finest EM excluding the coarser EM attributed to IRD inputs. The drawback of this method is that this EM ratio may simply reflect changes in sedimentary processes (e.g., changes in sources, turbidites) not related to current strength, in case the sediment is not well current-sorted (McCave & Andrews, 2019). The discrimination of the IRD components and the method to efficiently remove their potential contribution to grain size spectra are therefore not yet fully attained.

Recent studies suggest that the geochemical ratio Zirconium (Zr) to Rubidium (Rb) can be considered as a grain-size proxy recording flow speed variability in contouritic environments (Dypvik & Harris, 2001; Mirzaloo et al., 2019; Toucanne et al., 2021; L. Wu et al., 2020). Zirconium originates from heavy mineral species, particularly zircon, which is present in various magmatic and metamorphic rocks. It is widely distributed in natural sediments and, resistant to dissolution, it is in particular present in relatively coarse silty-sized fractions (L. Wu et al., 2020). In contrast, rubidium is mainly found in Potassium (K)-rich minerals. These minerals (e.g., K-feldspar, micas) are sensitive to chemical alteration and, in some environments, Rb variations may be influenced by continental weathering. Nevertheless, the Rb content is considered to illustrate the fine particle content (Dypvik & Harris, 2001). The Zr/Rb ratio may therefore be influenced by coarse silt delivered by iceberg, whilst the sandy-sized IRD fraction does not contribute to this ratio, as long as it is not composed of Zr-rich or Rb-rich lithic grains (L. Wu et al., 2020).

We propose here a new approach to quantify and correct the IRD influence on $\overline{SS}$. We check the $\overline{SS}$ records against the Zr/Rb ratio used as a reference for grain-size changes free of sandy IRD. After describing our method, we compare the results to those from the method of Jonkers et al. (2015), most currently-used to correct IRD inputs. Our procedure is illustrated for sediments under low flow speed conditions, with two sedimentary cores retrieved from different depths at different latitudes in the North Atlantic along the Reykjanes Ridge, and one core from the Antarctic margin (Figure 1) previously studied by L. Wu et al. (2020).

2. Regional, Oceanographical and Core Settings

To reach our goal, we investigate sedimentary cores under a persistent influence of deep sea currents, with both geochemical and grain-size data available, the latter covering the clay, silt and sand size fractions (from ~0 to >1,000 μm).

The two sedimentary cores from the subpolar North Atlantic (MD03-2679 and MD03-2673, Table 1) were collected during the MD132-P.I.C.A.S.S.O. cruise onboard the R.V. *Marion Dufresne* (Laj, 2003). These two cores recovered sediments from the Bjorn Drift and southern Gardar Drift, respectively, two sedimentary drifts located on the eastern flank of the Reykjanes Ridge (Figure 1). Sediment deposition in this area is under the influence of Iceland-Scotland Overflow Water (ISOW), one of the major component of the lower limb of the Atlantic Meridional Overturning Circulation (AMOC). This water mass is formed in the Nordic seas and flows southward passing over the Greenland-Scotland sill. Depending on its efficiency, ISOW remobilizes the sedimentary fraction originating from the surrounding basaltic regions and accumulated on the sill. This sediment, rich in magnetic grains, Titanium (Ti) and Iron (Fe)-rich particles, is then transported by ISOW to the open Atlantic ocean (Ballini et al., 2006; Grützner & Higgins, 2010; Kissel et al., 2009). The magnetic concentration and grain size measured in core-tops and Holocene sequences distributed along a latitudinal transect in this area decrease with the distance to the sill reflecting that it is the unique Northern detrital source, at least for this fraction (Kissel et al., 2009, 2013).

Both cores are characterized by light gray or olive gray silty lithofacies consistently with the description of sediments deposited and/or reworked by the persistent action of the ISOW bottom current (Bianchi & McCave, 2000; Mulder et al., 2013). Sedimentary cores in this area record a characteristic mixture of diatom (Shimada et al., 2008; Xuan et al., 2016) and IRD (Barker et al., 2015) layer during the Termination IV (Marine isotopic stage (MIS) 10-9 boundary), also present in these two cores. The presence of isolated horizons with sand to gravel-sized clasts suggests that both cores are moderately affected by iceberg rafting during the period of interest

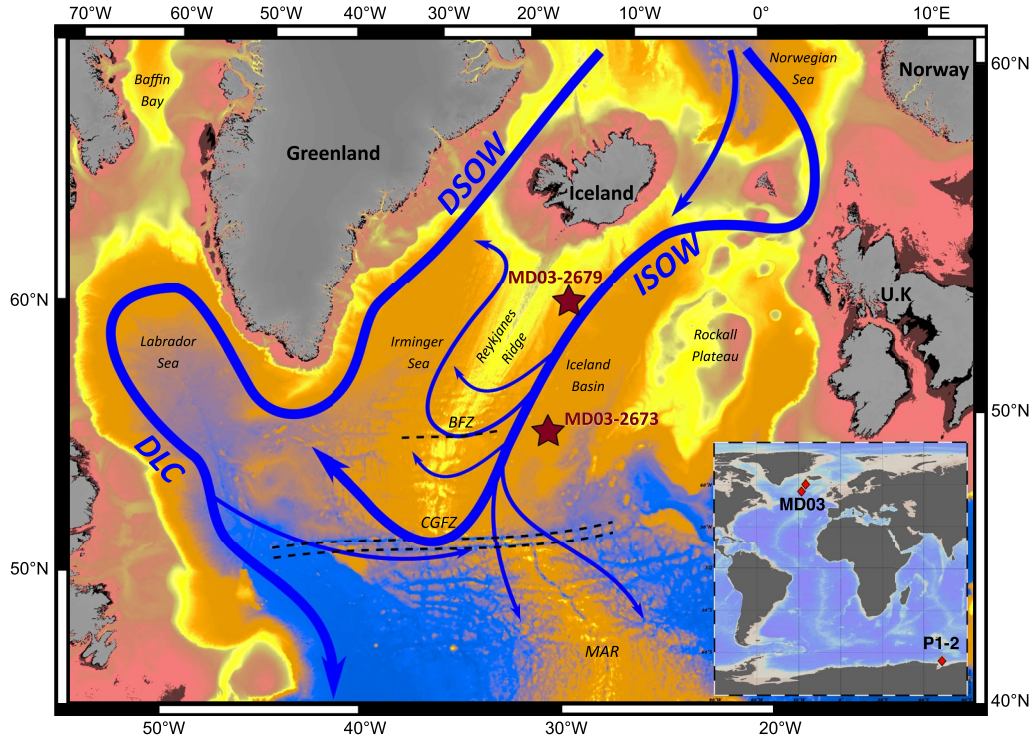

Figure 1. Bathymetric map of the North Atlantic region. Blue arrows are bottom-current flow pathways. Brown stars are the location of the two studied cores presented in this study. DSOW = Denmark Strait Overflow Water; ISOW = Iceland-Scotland Overflow Water; BFZ = Bright-Fracture Zone; CGFZ = Charlie-Gibbs Fracture Zone; MAR = Mid-Atlantic Ridge; UK = United Kingdom. The map in the lower right corner is a bathymetric map showing the locations of the three studied sites (red diamonds).

that extends between Termination IV and the end of MIS7. Sedimentation rates of previously studied cores along the Reykjanes ridge are varying between 5 and 20 cm ka^{-1} (Barker et al., 2015; Grützner & Higgins, 2010).

The third sedimentary core ANT30/P1-2 (L. Wu et al., 2018, 2020; labeled P1-2 by the authors) was retrieved from the lower continental slope of Prydz Bay, an embayment along the Antarctic margin between 66°E and 79°E (Table 1). It is composed of structureless clayey silt and silty clay, with a minor proportion of sand. The sedimentation rate is low and the sequence covers the last 520 ka over its length of 624 cm.

3. Analytical Methods

3.1. Grain-Size Analyses and Sortable Silt

Samples used for grain-size analyses in core P1-2 were treated with H_2O_2 (10%), HCl (1.0 N) and NaOH (2.0 N) in a bath at 85°C to remove organic carbon, carbonate and biogenic silica, respectively (L. Wu et al., 2020). The grain-size analyses were performed using a laser particle sizer *Beckman Coulter LS230* (L. Wu et al., 2020).

The grain-size distribution (GSD) of the lithogenic fraction of cores MD03-2679 and MD03-2673 was obtained using a laser diffraction particle-size analyzer *Malvern MasterSizer 2000* (101 size classes between 0.02 and 2,000 μm) at the GEOPS laboratory (University of Paris-Saclay, France) and *Malvern MasterSizer 3000* (101 size

Table 1
Core Locations

Site	Longitude (°E)	Latitude (°N)	Water depth (m)	Core length (m)	Data source
MD03-2679	−24.53	61.05	1,812	35.37	This study
MD03-2673	−27.81	56.37	2,786	39.05	This study
ANT30/P1-2	72.94	−65.01	2,860	6.24	L. Wu et al. (2020)

classes between 0.01 and 3,500 μm) at the LPG-BIAF laboratory (University of Angers, France), respectively. The biogenic carbonate, organic matter and silica (diatoms) were removed, prior to grain-size analyses for 265 samples from core MD03-2679 and 318 samples from core MD03-2673, distributed along MIS 7 and 9. All samples (2 cm^3) were decalcified at room temperature during 2 hr using acetic acid (20%) and rinsed three times with deionized water in the centrifuge at 3,000 rpm for 10 min. Subsequently, the samples were treated with ∼20 ml of hydrogen peroxide (33%) in a bath at 85°C during 2 hr to remove the organic matter, followed again by three rinsing. Finally, the opal was removed using 2*M* of sodium carbonate (50 ml) during 5 hr in a bath at 85°C, followed by three rinsing. Prior to grain-size measurements, 2 ml of a solution of sodium hexametaphosphate (Calgon, 2 g/L) was added to the sample, then placed in an ultrasonic tank during 2 min. The laser diffraction measurements were run in a deionized water tank with red light, Fraunhofer approximation and no ultrasound during the measurement in order not to warm up the solution and change its optical properties. Two parameters were calculated following previous studies: $\overline{SS}$, the geometric mean grain-size of the sortable fraction of silt (McCave et al., 1995) and SS%, the percent of non-cohesive silt (10–63 μm) divided by total percent of the fraction smaller than 63 μm (McCave & Hall, 2006). Both parameters were calculated according to McCave and Andrews (2019) by adding interpolated columns at 10 and 63 μm in grain-size datasets. A downcore linear correlation coefficient r_{run} was calculated between SS% and $\overline{SS}$ for all grain-size data using a sliding window of 9 points (McCave & Andrews, 2019). This "r_{run}" allows to detect intervals where the sediment is well current-sorted ($r > 0.5$). This test provides a first order indication of current sorting, but it is necessary to carefully examine rejected intervals in order to differentiate those with a clear trend of poorly sorted sediments from those influenced by a single outlier.

3.2. Zr/Rb Ratio as a Grain-Size Proxy

The elemental composition, including Zr and Rb contents, of the two North Atlantic cores discussed here were obtained using an *Avaatech* X-Ray Fluorescence (XRF) core scanner, which provides rapid, non-destructive and high-resolution records (Croudace & Rothwell, 2015; Croudace et al., 2019; Richter et al., 2006; Weltje & Tjallingii, 2008). The elemental composition of cores MD03-2679 and MD03-2673, reported here for the first time, were specifically analyzed using the 4th generation Avaatech core scanner of the Laboratoire des Sciences du Climat et de l'Environnement (LSCE). After a careful smoothing, the sediment surface was covered with an Ultralene® foil to avoid the contamination of the sensor. XRF data were collected every 1 cm with downcore and cross-core slits of 1 and 1.2 cm, respectively, throughout the entire length of the cores. The counting time was 10 s at 10 kV (no filter, under helium flow) for light elements and 30 kV (Pd thick filter, under air flow) for heavier elements, with an X-ray intensity of 140 and 90 μA, respectively. Three replicas were measured every 10 cm to estimate the measurement precision which is 3.4% and 5.1% for Zr, and 6.2% and 7.8% for Rb, in core MD03-2679 and MD03-2673, respectively. A certified standard SARM4 ("monitor scan") was measured at 10 kV between each section measurement in order to further ensure the reproducibility of the data and verify the presence of reliable technical conditions of measurement, such as the absence of helium leak which impacts light element measurements.

XRF core-scanning data are affected by specimen (e.g., variable water content, GSDs and presence of burrows) and matrix effects which impact the absorption, enhancement and scattering effects caused by the presence of other elements in a specimen (Weltje & Tjallingii, 2008). These effects on XRF semi-quantitative core-scanner data may be reduced by the use of a Multivariate Log-ratio Calibration (MLC, Weltje et al., 2015). To calibrate the XRF core-scanner data, we measured the elemental composition of discrete sediment samples using powder Energy Dispersive XRF. A total of 96 and 85 discrete samples for cores MD03-2679 and MD03-2673, respectively, was thus analyzed using the PANalytical Epsilon 3^{XLE} ED-XRF spectrometer available at LSCE. Discrete samples were selected from the XRF scanning profiles in order to cover the entire range of variations of 10 geochemical elements (see Supporting Information S1). All samples were measured with a counting time of 100 s at 5 kV (no filter, under helium flow), 12 kV (thick Al 50 μm filter, under air), 20 kV (thick Al 200 μm filter, under air) and 50 kV (Ag filter, under air) with X-ray intensities of 700, 320, 140, and 140 μA, respectively. More than 50% of samples were analyzed three times, to estimate the measurement precision (2.8% and 1.5% for Zr and 3.2% and 1.9% for Rb in cores MD03-2679 and MD03-2673, respectively). These discrete measurements were used to calibrate the core-scanner intensities of 10 geochemical elements (see Figures S1–S4 in Supporting Information S1 for more information) using the GUI Matlab® Xelerate (Weltje et al., 2015). As suggested by previous studies (Aitchison, 1990; Weltje et al., 2015; Weltje & Tjallingii, 2008), geochemical ratios are presented in log-ratios. The ln(Zr/Rb) of calibrated concentrations of raw core-scanner data and that of discrete samples shows significantly high correlations with $r = 0.86$ and $r = 0.78$ for cores MD03-2679 and MD03-2673, respectively (Figure 2), suggesting that the calibration is robust in both cores.

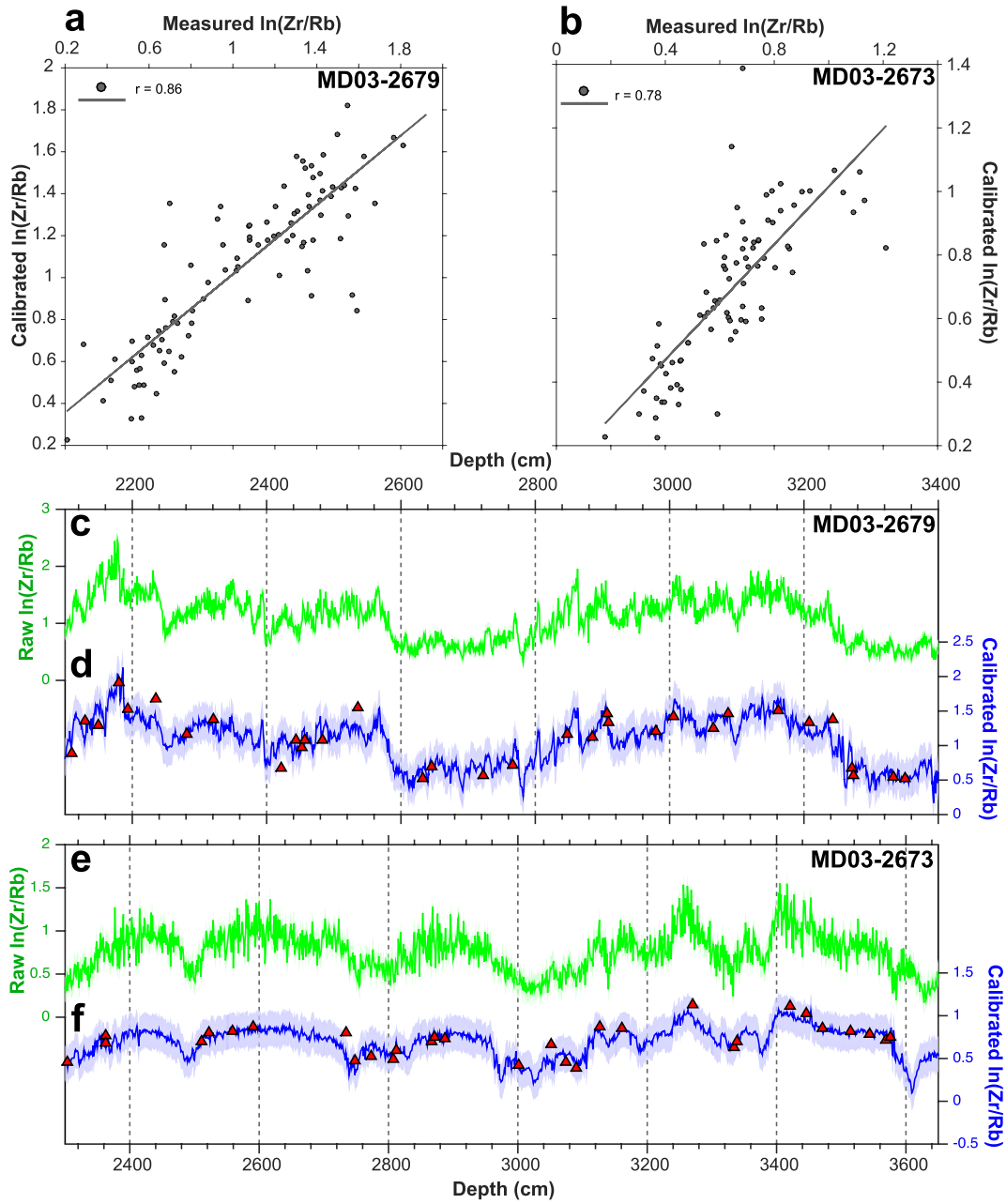

Figure 2. X-Ray Fluorescence Multivariate Log-ratio Calibration results for cores MD03-2679 and MD03-2673. (a) Linear correlation of ln(Zr/Rb) from measured (discrete samples) and calibrated (scanner) data of core MD03–2679 and (b) MD03-2673. Downcore profiles of raw core-scanner (green, c and e) and calibrated (blue, d, f) ln(Zr/Rb) of cores MD03-2679 and MD03-2673, respectively, with their respective 95% confidence intervals. Red triangles in (d) and (f) are ln(Zr/Rb) values obtained by ED-XRF on discrete samples.

4. Assessing the Relationships Between ln(Zr/Rb), $\overline{SS}$ and IRD

S. Wu et al. (2021) suggested that the very fine sand fraction (63–125 μm) may be current-sorted in the high hydrodynamical environment of the Drake Passage (current velocity between 40–60 cm s^{-1}; Donohue et al., 2016). This observation is reflected in grain-size modes around 63 μm in the Drake Passage (S. Wu et al., 2021). In contrast, the three cores from Gardar Drift and Prydz Bay exhibit finer GSDs (with main modes between 3 and 20 μm, Figure S5 in Supporting Information S1) than in the Drake Passage, in agreement with a lower bottom flow speed (e.g., current ISOW velocity between 3 and 20 cm s^{-1}; Thornalley et al., 2013; McCave et al., 2017). In addition,

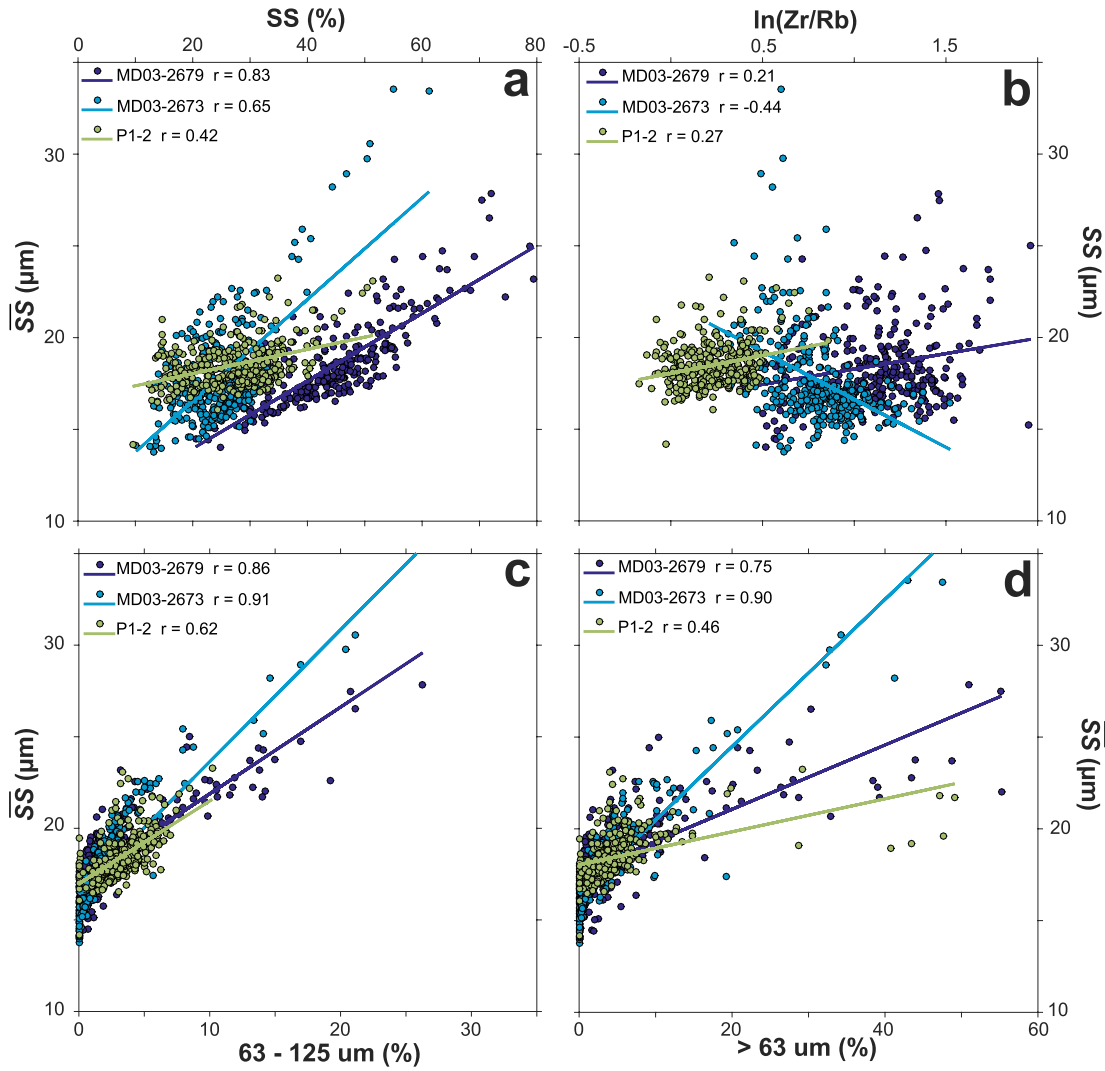

Figure 3. Linear correlations and correlation coefficients calculated between $\overline{SS}$ and (a) SS%, (b) ln(Zr/Rb) (c) very fine sand content (%) and (d) sand content (%) for the three studied cores.

most peaks of the entire sand fraction (i.e., >63 µm, including very fine sand grains) observed in Gardar Drift cores also contain coarse sand grains (as indicated by peaks in sand fractions >125, >250, and >500 µm, Figure S5 in Supporting Information S1). This result suggests that the very fine sand fraction is not current-sorted at our study sites and the whole sand content can be considered as IRD deposition.

In core P1-2, ln(Zr/Rb) correlates to SS% (r = 0.9, L. Wu et al., 2020). It also differs from the sand variations (>63 µm) (Figures 4g and 4i), with a correlation coefficient of 0.002 (L. Wu et al., 2020). This suggests that the ln(Zr/Rb) ratio can be considered as a silt/clay proxy free of sandy IRD influence (L. Wu et al., 2020). The $\overline{SS}$ and ln(Zr/Rb) are poorly correlated in this core (r = 0.002, L. Wu et al., 2020). Moreover, the correlation coefficients between $\overline{SS}$ and the very fine sand (63–125 µm) and sand (>63 µm) contents are 0.62 and 0.46 (Figures 3c and 3d), respectively, suggesting a moderate influence of IRD on $\overline{SS}$ values. Finally, the index sorting of 0.42 (Figure 3a) and the fact that 46% of the $\overline{SS}$ record is rejected by the r_{run} (gray areas in Figure 4h) indicate that the sediment in this core is generally not well current-sorted with persistent influences of high sand and IRD contents.

Core MD03-2679 is characterized by large variations in sand content (from 0 to >50%), most likely related to IRD input given the hemipelagic sedimentary context of the core (Figure 4c). The intervals between 2,100 and 2,200 cm and around 3,300 cm show clear peaks of high sand content, and intervals at 2,300–2,500 cm and 2,800–3,000 cm exhibit recurring sand peaks (Figure 4c). No obvious relationship is observed between changes in ln(Zr/Rb) (Figure 4a) and in sand content (Figure 4c), which suggests that ln(Zr/Rb) may be used as a silt/clay

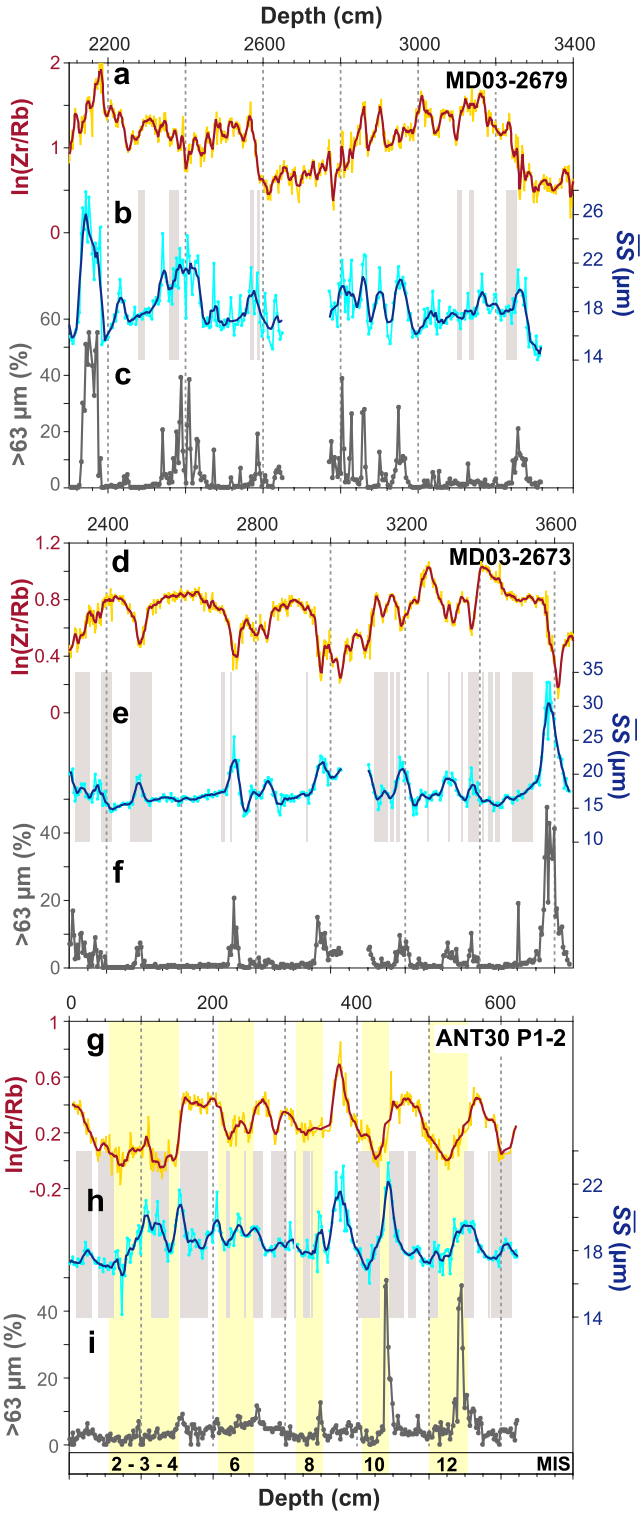

Figure 4. Downcore variations in (a, d, g) ln(Zr/Rb), (b, e, h) $\overline{SS}$ and (c, f, i) sand content (%) in cores MD03-2679 (a–c), MD03-2673 (d–f) and P1-2 (g–i). Gray areas are periods where the sediment is not current-sorted ($r_{run} < 0.5$). Yellow areas represent glacial periods covered by core P1-2 after L. Wu et al. (2018, 2020).

proxy free of sandy IRD influence. In contrast, the ln(Zr/Rb) record is not correlated with the $\overline{SS}$ record, which is, in turn, significantly correlated with the sand (>63 µm; $r = 0.75$) and very fine sand (63–125 µm; $r = 0.86$) contents (Figures 3c and 3d). Therefore, $\overline{SS}$ seems to be influenced by silt-size IRD derived particles. Regardless of this IRD influence on GSDs, the coefficient of correlation of 0.83 between $\overline{SS}$ and SS% (Figure 3a) suggests that the sediment is generally well current-sorted in this core. More specifically, only a few intervals (gray areas in Figure 4b) are rejected by the r_{run} test, and thus contain non-current-sorted sediment. Therefore, core MD03-2679 is composed of both current-transported and ice-rafted sediments.

The highest concentration in sand (up to 40%) in core MD03-2673 is around 3,600 cm corresponding to Termination IV (Figure 4f). This is a characteristic of cores from the Reykjanes Ridge (Barker et al., 2015; Mokeddem & McManus, 2017), which also corresponds to a diatom-rich layer (Shimada et al., 2008; Xuan et al., 2016). Because of the diatom ooze layer, XRF core-scanning may be biased by a strong specimen effect (inhomogeneity of surface and high water content). In this horizon, grain-size analyses may also be biased, due to the low quantity of fine-grained materiel after chemical treatments (e.g., removal of biogenic opal). The chemical treatment with Na_2CO_3 may not have entirely leached this type of diatom ooze and diatom shells might be included in the grain-size analyses. Due to all these incertainties of the data quality of this horizon, it will not be considered for further interpretations.

The intervals at 3,400 to 3,300, ~3,200, 2,950, 2,750, and below 2,400 cm are punctuated by moderate sand content (5%–20%) (Figure 4f). The ln(Zr/Rb) values are generally low during these sand intervals (Figures 4d–4f), while they are high during intervals with very low or no sand content. Thus, the ln(Zr/Rb) record is not influenced by sand content all along the record. In contrast, the $\overline{SS}$ record varies consistently with sand (Figures 4e and 4f) ($r = 0.90$; Figure 3d), very fine sand ($r = 0.91$; Figure 3c), and it seems to be anti-correlated with ln(Zr/Rb) variations ($r = -0.44$; Figures 3b, 4d, and 4e). All these observations show that the $\overline{SS}$ record is strongly influenced by silt-sized IRD in this core. Nevertheless, the $\overline{SS}$ versus SS% scatter plot reveals a coefficient of correlation of 0.65 (Figure 3a), characteristic of current-sorted sediments ($r > 0.5$). The whole $\overline{SS}$ record is punctuated by many intervals rejected by the r_{run} test (gray areas, Figure 4e), especially in the 3,100–3,550 interval. These rejected intervals suggest that $\overline{SS}$ may not be used as a current-strength proxy for about 28% of the total record. Therefore, core MD03-2673 is also composed of current-sorted sediments (but in a lesser extent than core MD03-2679) and is frequently affected by sand-rich IRD deposition.

In summary, the ln(Zr/Rb) ratio is considered and is used as a grain-size proxy free of sandy IRD influence in all three cores. Sediments are well current-sorted, moderately current-sorted and poorly current-sorted in cores MD03-2679, MD03-2673, and P1-2, respectively. Finally, the $\overline{SS}$ records are strongly influenced by silt-sized IRD in core MD03-2673 and moderately in cores MD03-2679 and P1-2. In light of these observations, an IRD correction is needed to reliably reconstruct past changes in bottom-current intensity.

5. Unmixing GSD to Correct the Influence of IRD

5.1. Defining a New Method to Correct the Influence of IRD

This method assumes that the GSD of hemipelagic sediments always contains a fine fraction of sediment sorted by bottom currents, and occasionally

coarse-grained fractions related to IRD. With this hypothesis in mind, isolating the GSD associated with the current-transported fraction and recalculating it in sum to 100% produces a modified GSD free of IRD influence.

Our method is focused on the removal of the IRD influence from the entire GSD to construct a modified GSD matrix using the parametric EMA of the GUI Matlab AnalySize (Paterson & Heslop, 2015). Generally, EMA aims to fix the minimum number of EM related to mixing dynamics that represents a sufficient percentage of the variance (e.g., Dietze et al., 2012; Paterson & Heslop, 2015; Weltje, 1997). Here, we have decided to use parametric EMA to deconvolve the GSD with the highest number of EM. This high number of EM allows a better representation of the initial GSD than the use of only two or three EM, especially for samples with plurimodal distributions due to IRD content. The AnalySize GUI Matlab supports four types of parametric distributions (Paterson & Heslop, 2015). The Skewed Generalized Gaussian (SGG) and Lognormal parametric distributions do not control the shape of distributions (Paterson & Heslop, 2015). The General Weibull distribution adds an additional location parameter to the Weibull distribution (which have parameters controlling the shape and the scale of the distribution) and produces EM with a larger left-hand tail than Weibull distributions (Paterson & Heslop, 2015). As our new method needs Gaussian shape and well-constrained EM in term of grain-size range, we decided to run EMA with Weibull distributions. The distributions represented by the sum of all EM distributions deduced from the Weibull EMA approach covers more than 99% of the original GSD for the large majority of datasets used in this study.

Then, we group some of the defined EM in order to isolate the current-sorted fraction (hereafter labeled EM_{CS}) from the coarse "IRD" fraction (hereafter labeled EM_{IRD}) (Figure 5). The difficulty is to decide which EM represents particles transported and sorted by bottom currents and which EM represents grains derived from ice or iceberg rafting. For all cores, the EM_{CS} are always identified in GSD of samples with no IRD influence (e.g., Figures 5a and 5b). We noticed that the percentile 80 (P80) of the average GSD of each core could be a grain-size limit between the two EM groups (Table 2, Figures S5a, S5c, and S5e in Supporting Information S1). EM with a median grain-size higher than the P80 value of the core are placed in the EM_{IRD} group, while those with a median grain size below the P80 value belong to the EM_{CS} group. This P80 limit is reliable for the studied cores but it might not be always the case, so we encourage users to first closely examine EM composing the unimodal distributions of current-sorted samples.

In the following, we shall describe, step by step the new approach we propose to correct GSD from the influence of IRD. Note that we produced a MATLAB script (available at https://gitlab.in2p3.fr/nathan.stevenard/ird_corr_package) to facilitate the application of this method.

After running the EMA and defining the n number of EM related to EM_{CS} (see above), the first step of our method is to calculate, for each sample, the GSD of each EM in a structure X using their abundances (*EMa*) and their densities (*EMd*) following the equation:

$$X_{j,k,i} = \frac{EMd_{k,i} * EMa_{j,i}}{100}$$

where i is the ith EM, j is the jth specimen (sample) and k is the kth grain-size bin. This equation gives a X structure with $\{1, 2,\ldots, i-1, i\}$ matrixes composed of $\{1, 2,\ldots, j-1, j\}$ rows (specimens) and $\{1, 2,\ldots, k-1, k\}$ columns (grain-size bins).

The next step is a simple addition of n matrixes of X into a single matrix to obtain a modified GSD Y free of IRD influence for each specimen. This modified GSD will be composed by $\{X_1 + X_2 + \ldots + X_{n-1} + X_n\}$ matrixes from the X structure:

$$Y_{j,k} = \sum_{i=1}^{n} X_{j,k,i}$$

Now that we have removed the percentages of GSD containing EM_{IRD}, we recalculate the grain-size volume percentages of the matrix Y so that they sum to 100% in the modified GSD (*ModifiedGSD*):

$$ModifiedGSD_{j,k} = \frac{Y_{j,k} * 100}{\sum_k Y_{j,k}}$$

At this step, the GSD correction of IRD contributions is done and we constructed a modified GSD free of IRD influences from which we can now calculate any grain-size parameter (e.g., sorting, skewness, kurtosis) as well as the IRD-corrected sortable silt parameters $\overline{SS}_{IRD\_free}$ and $SS\%_{IRD\_free}$ following the method described in Section 3.1.

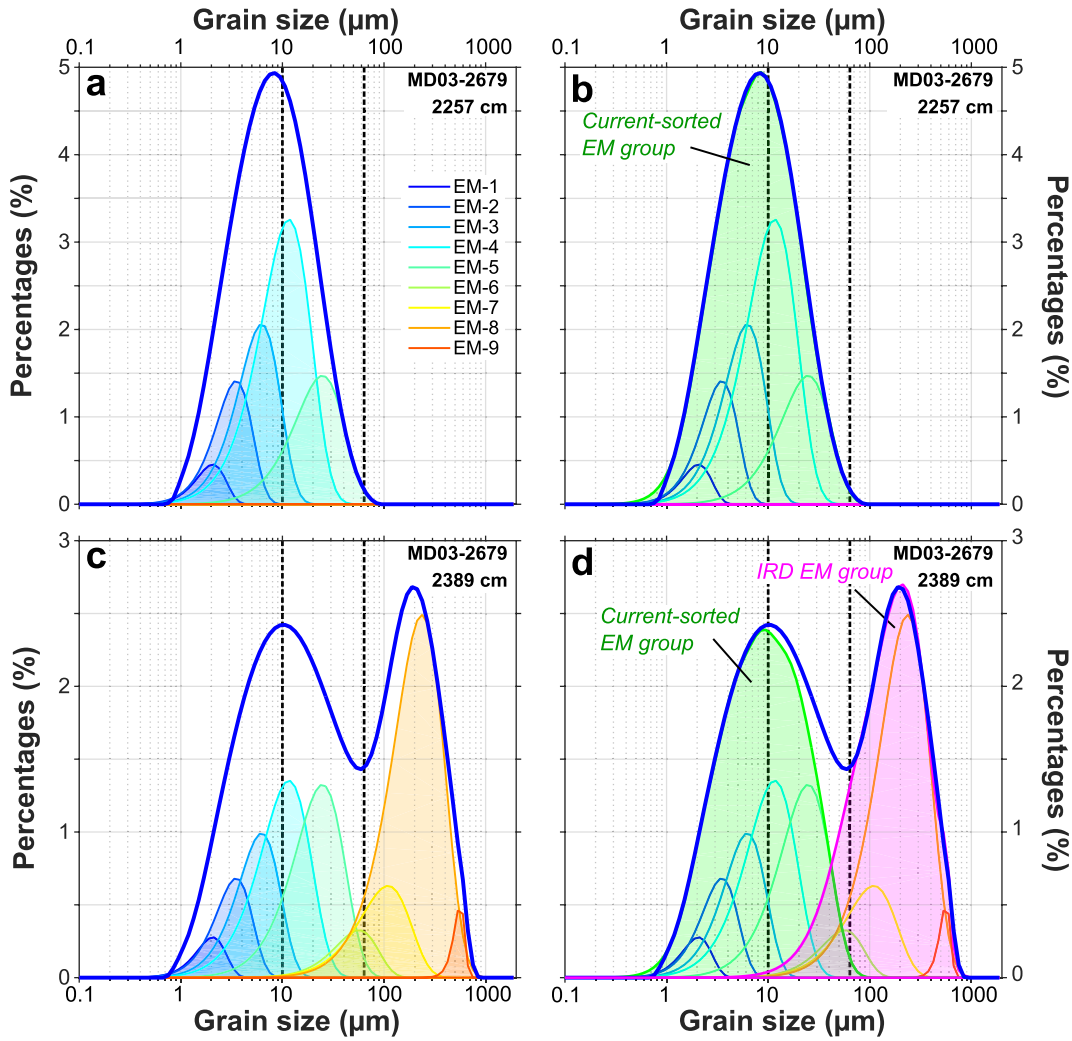

Figure 5. Grain-size distribution of two representative samples from core MD03-2679 with their End-Members (EM) distributions (a, c) and their EM_{CS} and EM_{IRD} groups (b, d). (a, b) Sediment with no Ice-Rafted Detritus (IRD) influence; (c, d) Sediment with a strong IRD contribution. Black dashed lines marked the interval 10–63 μm.

5.2. Applications of the New Method to the Studied Sedimentary Cores

This section compares the new grain-size parameters ($\overline{SS}_{IRD\_free}$, $SS\%_{IRD\_free}$, sorting index, r_{run}) with ln(Zr/Rb) and the original $\overline{SS}$ described in Section 4.

The three cores now exhibit $\overline{SS}_{IRD\_free}$ variations which are more consistent with ln(Zr/Rb) records than the original $\overline{SS}$ profiles (Figure 6). Sorting indexes and correlation coefficients between ln(Zr/Rb) and $\overline{SS}_{IRD\_free}$

Table 2
Percentile 80 of the Studied Cores and Medians of Their Associated EM

		Median (μm)									
Core name	P80 (μm)	EM1	EM2	EM3	EM4	EM5	EM6	EM7	EM8	EM9	EM10
MD03-2679	21.19	1.68	2.99	5.32	9.46	21.19	47.43[a]	84.34[a]	188.81[a]	532.15[a]	–
MD03-2673	11.20	0.81	1.44	2.89	5.72	10.97	11.03	28.38[a]	82.48[a]	166.40[a]	–
ANT30/P1-2	14.26	2.01	5.11	8.15	12.99	27.39[a]	92.09[a]	121.80[a]	282.10[a]	–	–

[a]Highlights EM considered as IRD for each core.

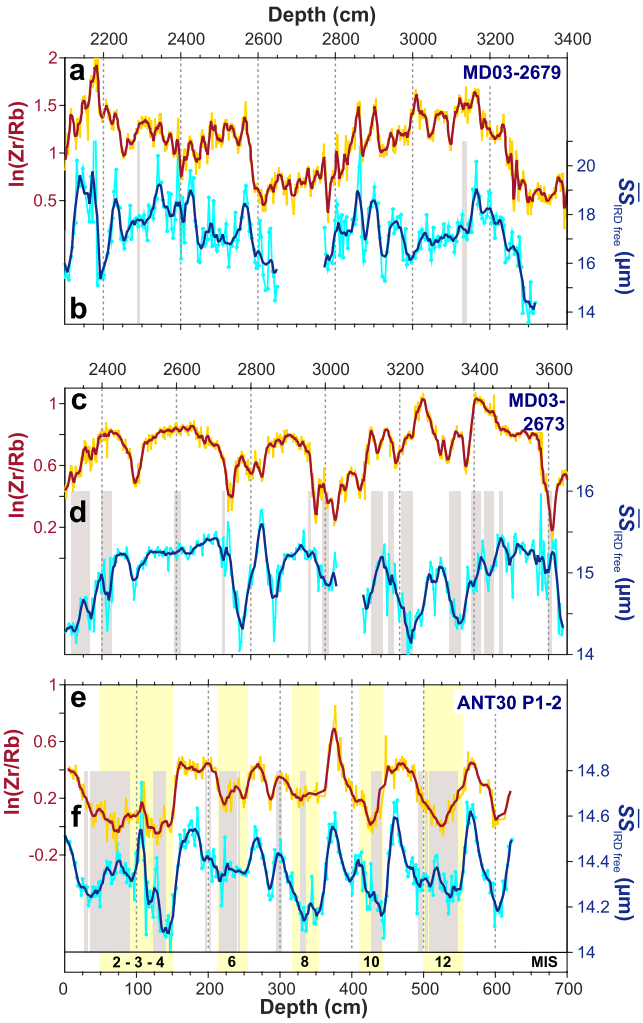

Figure 6. Downcore variations in (a, c, e) ln(Zr/Rb) and (b, d, f) $\overline{SS}_{IRD\_free}$ for cores (a, b) MD03-2679, (c, d) MD03-2673 and (e, f) P1-2. Gray areas are periods where the sediment is not current-sorted ($r_{run} < 0.5$). Yellow areas represent cold periods covered by core P1-2 after L. Wu et al. (2018, 2020).

also improve with respect to the original correlations (Figure 7). Moreover, intervals rejected by the r_{run} are fewer after correction than before (Figure 6).

In greater detail, the grain-size data of core P1-2 were decomposed into eight EM with the Weibull parametric EMA. With a P80 value of 14.26 µm (Table 2), four EM were kept in the EM_{CS} group, and four in the IRD EM_{IRD} group. The sorting index increases from 0.42 to 0.64 (Figure 7c) and the correlation coefficient between ln(Zr/Rb) and $\overline{SS}_{IRD\_free}$ also increases from 0.27 to 0.58 (Figure 7d). The few intervals rejected by the new r_{run} (gray areas in Figure 6f) suggest oceanographic changes (e.g., changes of the depth or latitude of the deep current) rather than changes in bottom current strength. L. Wu et al. (2020) correlated the ln(Zr/Rb) values with each grain-size bin and showed that the ratio is negatively correlated with the <7 µm fraction and positively correlated with the 8–63 µm fraction (Figure 8c in L. Wu et al., 2020). These correlations suggest that the ln(Zr/Rb) ratio can be used as a ratio of non-cohesive versus cohesive sediment fractions. We do not exlude a possible influence of chemical weathering effet on this ratio. However, such a ratio resembles the calculation mode of SS%, rather than of $\overline{SS}$. $\overline{SS}_{IRD\_free}$ and $SS\%_{IRD\_free}$ are different in this core during glacial period ($r_{run} < 0.5$) and this "low" correlation between $\overline{SS}_{IRD\_free}$ and ln(Zr/Rb) is understandable for the Antarctic margin for these intervals.

The GSD in core MD03-2679 has been decomposed into nine EM with Weibull parametric EMA. The P80 value of the average GSD is 21.19 µm (Table 2). This suggests to keep five EM and four EM in the EM_{CS} and EM_{IRD} groups, respectively (Table 2). The long-term trend between ln(Zr/Rb) and $\overline{SS}_{IRD\_free}$ records is generally the same. The sorting index increases from 0.83 to 0.93 (Figure 7a) and the correlation coefficient between ln(Zr/Rb) and $\overline{SS}_{IRD\_free}$ also increases from 0.21 to 0.49 (Figure 7b). Only two intervals are rejected by the r_{run} (gray areas in Figure 6b) after the correction of IRD contribution. Also, $\overline{SS}_{IRD\_free}$ does not increase anymore or increases less abruptly in intervals with high sand content (Figure 4c). Thus, these observations strongly suggest that the modified GSD used to calculate SS_{IRD_free} is indeed free of IRD influence.

The GSD of the last core MD03-2673 have been decomposed into nine EM with Weibull parametric EMA (Table 2). The very low P80 value of 11.2 µm indicates that the first six EM were retained for the EM_{CS} group and the remaining three for the EM_{IRD} group (Table 2). Intervals around 3,600, 3,300–3,400, 3,200, 2,950, 2,750, and below 2,400 cm, where sand values were originally high, show no obvious peaks of $\overline{SS}_{IRD\_free}$ values. The long-term trend is generally consistent between $\overline{SS}_{IRD\_free}$ and ln(Zr/Rb) records (Figures 6c and 6d). The coefficient of correlation between both tracers increases from −0.44 to 0.18 after the IRD correction (Figure 7d). The index sorting increases from 0.65 to 0.79 (Figure 7c) and few intervals are rejected by the new r_{run} (gray areas in Figure 6d). Note that these rejections are often due to only one or two outliers. For example, the three rejected intervals between 3,400 and 3,500 cm ($n = 24$) show that 71% of data (17 $\overline{SS}$ values) are rejected by the test. If two points considered as outliers are removed, the percentage of rejected data drops to 17% (4 $\overline{SS}$ values).

In summary, by applying our new method, we increase the correlations between $\overline{SS}_{IRD\_free}$, $SS\%_{IRD\_free}$ and ln(Zr/Rb) and decrease the number of intervals rejected by the r_{run}. In the three cores, no obvious peaks of $\overline{SS}_{IRD\_free}$ occur any more in intervals where the sand content is high. In our approach, IRD with a grain-size bigger than the EM_{CS} grain-size range are considered as unsorted, whereas IRD finer than the EM_{IRD} grain-size range are considered as current-sorted. The contribution of the EM_{IRD} is therefore removed in IRD-free GSDs, also in the grain-size interval where it overlaps the EM_{CS} group. According to McCave and Andrews (2019), particles within this overlapping grain-size range, whatever their origin, should also be sorted by bottom currents. However, this range of overlap corresponds to the tails of GSDs of the two EM groups (Figure 5d). It is short and covers a limited

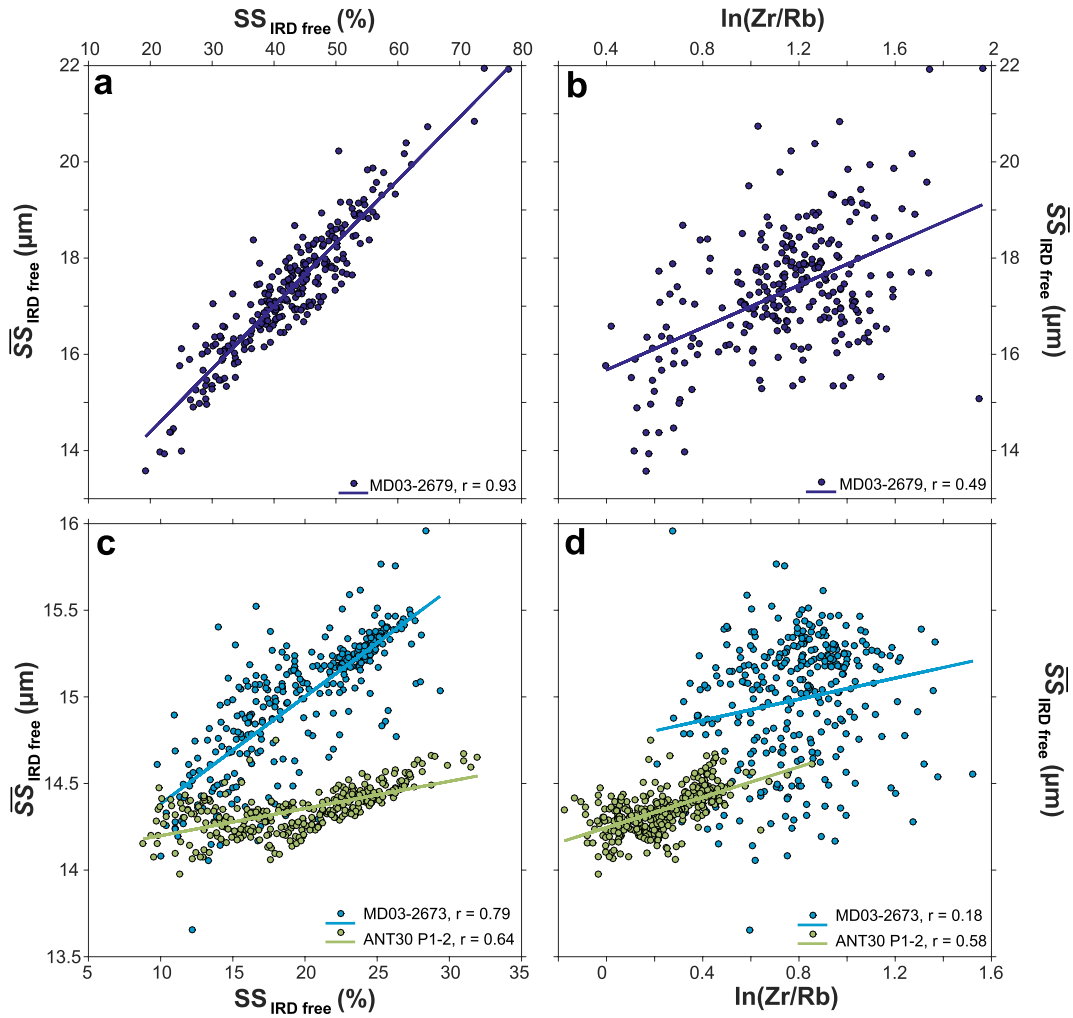

Figure 7. $\overline{SS}_{IRD\_free}$ versus SS_{IRD_free} (%) linear correlation for cores (a) MD03-2679, (c) MD03-2673 and P1-2, and $\overline{SS}_{IRD\_free}$ versus ln(Zr/Rb) for cores (b) MD03-2679, (d) MD03-2673 and P1-2.

area, compared to the two main components, EM_{CS} and EM_{IRD}. If the EM_{CS} group is biased by the removal of the EM_{IRD} in this area, it is toward lower EM_{CS} grain-size values. This effect seems to be limited in our case studies, but one has to keep in mind this methodological limit of the decomposition in EM. More importantly, the upper limit of the sortable fraction and the lower limit of pure vertically advected IRD, which strongly depend on the hydrodynamical energy of the deposition environment, are defined by the decomposition in EM itself. Our method, therefore, efficiently corrects GSD for IRD contributions. In the case study of the three studied cores from the North Atlantic and Prydz Bay, it provides a new paleo-current strength proxy free of IRD influence.

6. Comparison With the Method of Jonkers et al. (2015)

In order to better evaluate our new method, we now compare the results with those obtained with the non-parametric EMA method developed by Jonkers et al. (2015) and used in many studies (e.g., Hoffmann et al., 2019; McCave & Andrews, 2019; L. Wu et al., 2018). As a reminder, the tracer used for bottom-current intensity free of IRD influence in the non-parametric EMA is a log-ratio of the two finest EM (considering the coarser EM as IRD). We applied this method on the three studied cores and compare the EM log-ratio with our $SS\%_{IRD\_free}$ and $\overline{SS}_{IRD\_free}$ (Figure 8).

Core MD03-2679 has three EM produced by non-parametric EMA (Figure 8a). The first EM (EM1) is unimodal and mainly associated with the cohesive fraction, with a mode at 5 µm and a short fraction of the GSD in

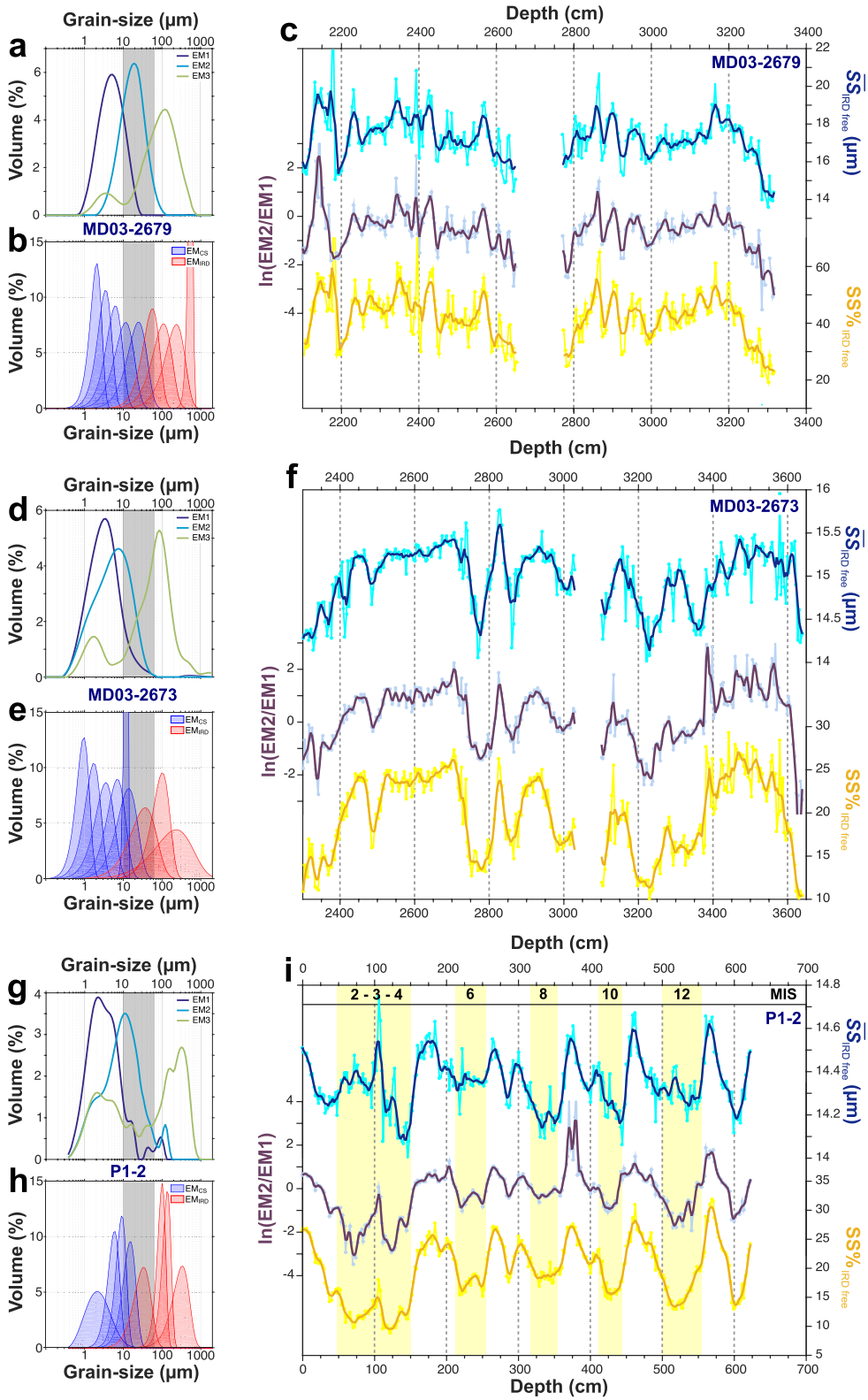

Figure 8.

the non-cohesive fraction up to 23 μm (Figure 8a). The second unimodal EM (EM2) mainly represents the non-cohesive silt fraction, extending from 2 to 100 μm with a mode at 20 μm (Figure 8a). The last bimodal EM (EM3) is associated with IRD. It covers grain-sizes ranging from 1 to 800 μm, and has two modes, a major one at around 100 μm and a secondary one at 4 μm (Figure 8a). With our method, the two groups of EM, EM_{CS} and EM_{IRD}, range from 0.3 to 100 μm and 4–900 μm, respectively (Figure 8b). The three tracers generally show the same variations (Figure 8c). Minor discrepancies (mainly in terms of amplitude) are observed around 3,150 cm, where ln(EM2/EM1) and $SS\%_{IRD\_free}$ increase while $\overline{SS}_{IRD\_free}$ decreases, and above 2,250 cm. The latter is also the sole interval where ln(EM2/EM1) differs from both $\overline{SS}_{IRD\_free}$ and $SS\%_{IRD\_free}$. It is characterized by a very high sand content (>50%) and therefore a high content of EM3 (whose downcore changes follow those of sand content, not shown). Due to a fine mode at 4 μm in EM3 (Figure 8a), the high EM3 abundance above 2,250 cm makes the abundance of EM1 and EM2 very low, and thus the ln(EM2/EM1) ratio inaccurate. Nevertheless, ln(EM2/EM1) is generally consistent with $SS\%_{IRD\_free}$ and $\overline{SS}_{IRD\_free}$. Since EM1 and EM2 are associated with the cohesive (<10 μm) and the non-cohesive (10–63 μm) fractions, respectively (Figure 8a), their ratio is close to the definition of SS%. And because the sediment of this core is very well current-sorted (i.e., $\overline{SS}_{IRD\_free}$ and $SS\%_{IRD\_free}$ vary closely together along the core), downcore changes in ln(EM2/EM1) also follow $\overline{SS}_{IRD\_free}$ variations. In summary, as the sediment is very well current-sorted in this core, the EM log-ratio exhibits the same variations as the $SS\%_{IRD\_free}$ and $\overline{SS}_{IRD\_free}$ records and all three can be used as a current-strength proxy in this core.

The non-parametric EMA of core MD03-2673 also decomposes the GSD into three EM (Figure 8d). EM1 is unimodal, ranging from 0.3 to 70 μm with a mode between 3 and 4 μm. EM2 is also unimodal, extending also from 0.3 to 70 μm, but with a mode at 8 μm. EM3, attributed to IRD, ranges from 0.3 to more than 2,000 μm. This EM is bimodal with a principal mode at 85 μm and a secondary one at 2 μm (Figure 8d). The EM_{CS} and EM_{IRD} groups produced by our new method range from 0.1 to 63 μm and from 1 to more than 2,000 μm, respectively (Figure 8e). The ln(EM2/EM1) profile shows downcore variations similar to those of $SS\%_{IRD\_free}$ (Figure 8f). They are also similar to $\overline{SS}_{IRD\_free}$ variations except for the interval 3,400–3,250 cm and above 2,400 cm (Figure 8f). The sediment of this core is less well current-sorted than in core MD03-2679, thereby inducing differences between the $SS\%_{IRD\_free}$ and $\overline{SS}_{IRD\_free}$ records. Even if EM1 and EM2 cover the same grain-size ranges (from 0.3 to 70 μm), their mode and distribution shapes differ (Figure 8d). Although it is less evident than for core MD03-2679, EM1 and EM2 of core MD03-2673 could also be associated with the cohesive and non-cohesive fractions, respectively, explaining why that ln(EM2/EM1) variations better follow $SS\%_{IRD\_free}$ than $\overline{SS}_{IRD\_free}$ changes (Figure 8f). Therefore, the EM2/EM1 log-ratio may only be used as current-strength proxy in this core when the sediment is well current-sorted.

The non-parametric EMA of the last core P1-2 reveals three EM (Figure 8g). EM1 has a multimodal distribution, ranging from 0.4 to 105 μm, with a principal mode at 2 μm and three others at 18, 45, and 90 μm (Figure 8g). EM2 is represented by a bimodal distribution between 0.4 and 200 μm, with a principal mode at 11 μm and a secondary one at ∼100 μm. EM3, considered as IRD, has a grain-size range from 0.4 to 1,000 μm, with a principal mode at 300 μm and a large mode covering the fine to very fine silt and clay fractions (Figure 8g). The EM_{CS} and EM_{IRD} groups obtained by parametric Weibull EMA, which are composed of four EM ranging from 0.4 to 40 μm and 3–1,000 μm, respectively (Figure 8h), have more distinct grains-size ranges. The parametric EMA constrains the EM shape unlike non-parametric EMA. The effect of this difference is very clear in this core with large overlaps between the non-parametric EM grain-size spectra (Figure 8g). The ln(EM2/EM1) profile shows variations similar to $SS\%_{IRD\_free}$ changes all along the core, and sometimes to $\overline{SS}_{IRD\_free}$ changes, mainly during interglacial periods when the sediment is current-sorted (blank areas in Figure 8i), except for MIS 11. This result suggests again that ln(EM2/EM1) represents a ratio of the non-cohesive to cohesive fractions rather than a strict current-strength proxy. Consequently, also in this core, the EM log-ratio can only be used as a current-strength proxy at times when the sediment is current-sorted.

Figure 8. Comparison of our grain-size distribution correction method of IRD influence to the one by Jonkers et al. (2015) for the three studied cores. (a, d, g) Non-parametric End-Member Analysis (EMA), (b, e, h) Weibull parametric EMA and (c, f, i) $\overline{SS}_{IRD\_free}$, ln(EM2/EM1) and $SS\%_{IRD\_free}$ profiles. (a–c) Core MD03-2679, (d–f) core MD03-2673 and (g–i) core P1-2. Gray areas on EMA panels represent the 10–63 μm fraction. Yellow areas on panel (i) are glacials periods after L. Wu et al. (2020). Note: the fifth End-Members (EM) (in blue) in panel (e) corresponds to overestimation of the number of EM of the EMA and is negligible due to its shape and its very low abundance (below 1%) along the core.

These three case-studies establish the limitations and conditions of use of the ln(EM2/EM1) ratio proposed by Jonkers et al. (2015) as a current-strength proxy free of IRD influences. In summary, the ln(EM2/EM1) ratio reflects a ratio of non-cohesive to cohesive fractions, similarly to $SS\%_{IRD\_free}$ changes. Thus, the EM log-ratio can only be used as a current-strength proxy when the sediment is well current-sorted (i.e., in case of a high correlation between $SS\%_{IRD\_free}$ and $\overline{SS}_{IRD\_free}$). This information about sediment sorting requires the calculation of both SS% and $\overline{SS}$ records on IRD-free GSD, and our method is the only one that gives this possibility.

7. Conclusions

In this paper, in the light of a new method, we examined the GSD of three hemipelagic sedimentary cores from the subpolar North Atlantic and the Antarctic margin, in order to provide the following conclusions:

1. The $\overline{SS}$ of very fine hemipelagic sediments can be strongly influenced by silt-sized IRD.
2. The EM log-ratio issued from the commonly used non-parametric EMA method can be used as a current-strength proxy only if the sediment (free of IRD) is well current-sorted. However, this information about current sorting (i.e., degree of correlation between $SS\%_{IRD\_free}$ and $\overline{SS}_{IRD\_free}$) is not accessible with this method.
3. The method proposed here, which is based on parametric EMA, allows deconvolution of current-sorted from IRD EM, thus creation of a modified GSD free of unsorted IRD influence, and calculation of grain-size parameters (e.g., mean, median, kurtosis, skewness) and SS% and $\overline{SS}$ records free of unsorted IRD influence.
4. The upper grain-size limit of the sortable fraction (identical to the lower limit of vertically advected IRD) varies according to hydrodynamical strength conditions of deposition environments.
5. This new method is the only one documenting the degree of sediment sorting independent of the IRD content, and thus establishing whether the different tracers are strict proxies for bottom-current strength or not.

In many cases, the $\overline{SS}$ proxy can be used without any grain-size correction. However, in specific environments, our method allows to define grain-size corrections, that either lowers the upper limit of the sortable silt range or may increases it, (thus extending the $\overline{SS}$ grain-size range), depending on hydrological strength conditions.

Data Availability Statement

The Matlab code of the method described in this study is available at https://gitlab.in2p3.fr/nathan.stevenard/ird_corr_package (Stevenard, 2023). Geochemical ratio ln(Zr/Rb) grain-size proxy and grain-size data of cores MD03-2679 and MD03-2673 used in this are available in the PANGAEA database Stevenard et al. (2023a, 2023b, 2023c, 2023d). Geochemical ratio ln(Zr/Rb) grain-size proxy and data of core ANT30-P1-2 used in this study are available in L. Wu et al. (2020) via L. Wu (2020).

Acknowledgments
We are grateful to the chief scientist (C. Laj) and the crew of the R.V. *Marion Dufresne* for collecting cores during the P.I.C.A.S.S.O cruise. We thank G. Maillet, M. Mojtahid (LPG-BIAF) and C. Skonieczny (GEOPS) for technical support for grain-size analyses and C. Wandres (LSCE) for technical support for XRF core-scanning. We are grateful to Prof. N. McCave for fruitful exchanges. N.S. acknowledges a PhD grant from the Commissariat à l'Energie Atomique et aux Energies Alternatives (CEA). A.G. acknowledges support from ANR (Grant ANR-18-BELM-0001-06). This work was supported by the CEA, the Centre National de la Recherche Scientifique (CNRS) and by the French National program LEFE (Les Enveloppes Fluides et l'Environnement), under the project DECORATING (Dynamique des principaux courants profonds de l'Atlantique lors des périodes chaudes du passé: étude des interglaciaires des derniers 450 000 ans). We would like to thank the associate editor and three anonymous reviewers for their valuable comments, which helped us to improve the quality of our manuscript.

References

Aitchison, J. (1990). Relative variation diagrams for describing patterns of compositional variability. *Mathematical Geology*, *22*(4), 487–511. https://doi.org/10.1007/BF00890330

Andrews, J. (2000). Icebergs and iceberg rafted detritus (IRD) in the North Atlantic: Facts and assumptions. *Oceanography*, *13*(3), 100–108. https://doi.org/10.5670/oceanog.2000.19

Andrews, J. T., & Principato, S. M. (2002). Grain-size characteristics and provenance of ice-proximal glacial marine sediments. *Science Progress*, *203*(1), 305–324. https://doi.org/10.1144/GSL.SP.2002.203.01.16

Ballini, M., Kissel, C., Colin, C., & Richter, T. (2006). Deep-water mass source and dynamic associated with rapid climatic variations during the last glacial stage in the North Atlantic: A multiproxy investigation of the detrital fraction of deep-sea sediments. *Geochemistry, Geophysics, Geosystems*, *7*(2), 16. https://doi.org/10.1029/2005GC001070

Barker, S., Chen, J., Gong, X., Jonkers, L., Knorr, G., & Thornalley, D. (2015). Icebergs not the trigger for North Atlantic cold events. *Nature*, *520*(7547), 333–336. https://doi.org/10.1038/nature14330

Bianchi, G. G., & McCave, I. N. (2000). Hydrography and sedimentation under the deep western boundary current on Björn and Gardar Drifts, Iceland Basin. *Marine Geology*, *165*(1–4), 137–169. https://doi.org/10.1016/S0025-3227(99)00139-5

Croudace, I. W., Löwemark, L., Tjallingii, R., & Zolitschka, B. (2019). High resolution XRF core scanners: A key tool for the environmental and palaeoclimate sciences. *Quaternary International*, *514*, 1–4. https://doi.org/10.1016/j.quaint.2019.05.038

Croudace, I. W., & Rothwell, R. G. (Eds.) (2015)., *Micro-XRF studies of sediment cores: Applications of a non-destructive tool for the environmental sciences, developments in paleoenvironmental research*. Springer.

Dietze, E., Hartmann, K., Diekmann, B., IJmker, J., Lehmkuhl, F., Opitz, S., et al. (2012). An end-member algorithm for deciphering modern detrital processes from lake sediments of Lake Donggi Cona, NE Tibetan Plateau, China. *Sedimentary Geology*, *243–244*, 169–180. https://doi.org/10.1016/j.sedgeo.2011.09.014

Donohue, K. A., Tracey, K. L., Watts, D. R., Chidichimo, M. P., & Chereskin, T. K. (2016). Mean Antarctic circumpolar current transport measured in Drake passage. *Geophysical Research Letters*, *43*(22), 11–760. https://doi.org/10.1002/2016GL070319

Dypvik, H., & Harris, N. B. (2001). Geochemical facies analysis of fine-grained siliciclastics using ThrU. *ZrrRb and žZr q Rb/rSr ratios*, *181*(1–4), 131–146. https://doi.org/10.1016/S0009-2541(01)00278-9

Grützner, J., & Higgins, S. M. (2010). Threshold behavior of millennial scale variability in deep water hydrography inferred from a 1.1 Ma long record of sediment provenance at the southern Gardar Drift. *Paleoceanography*, *25*(4), 17. https://doi.org/10.1029/2009PA001873

Hass, H. C. (2002). A method to reduce the influence of ice-rafted debris on a grain size record from northern Fram Strait, Arctic Ocean. *Polar Research*, *21*(2), 299–306. https://doi.org/10.3402/polar.v21i2.6491

Hoffmann, S. S., Dalsing, R. E., & Murphy, S. C. (2019). Sortable silt records of intermediate-depth circulation and sedimentation in the southwest Labrador sea since the last glacial maximum. *Quaternary Science Reviews*, *206*, 99–110. https://doi.org/10.1016/j.quascirev.2018.12.028

Jonkers, L., Barker, S., Hall, I. R., & Prins, M. A. (2015). Correcting for the influence of ice-rafted detritus on grain size-based paleocurrent speed estimates. *Paleoceanography*, *30*(10), 1347–1357. https://doi.org/10.1002/2015PA002830

Kissel, C., Laj, C., Mulder, T., Wandres, C., & Cremer, M. (2009). The magnetic fraction: A tracer of deep water circulation in the North Atlantic. *Earth and Planetary Science Letters*, *288*(3–4), 444–454. https://doi.org/10.1016/j.epsl.2009.10.005

Kissel, C., Van Toer, A., Laj, C., Cortijo, E., & Michel, E. (2013). Variations in the strength of the North Atlantic bottom water during Holocene. *Earth and Planetary Science Letters*, *369–370*, 248–259. https://doi.org/10.1016/j.epsl.2013.03.042

Laj, C. (2003). *MD 132/P.I.C.A.S.S.O.-IMAGES11 cruise*. Marion Dufresne R/V. https://doi.org/10.17600/3200050

Lamy, F., Arz, H. W., Kilian, R., Lange, C. B., Lembke-Jene, L., Wengler, M., et al. (2015). Glacial reduction and millennial-scale variations in Drake Passage throughflow. *Proceedings of the National Academy of Sciences of the United States of America*, *112*(44), 13496–13501. https://doi.org/10.1073/pnas.1509203112

Li, G., & Piper, D. J. W. (2015). The influence of meltwater on the Labrador Current in Heinrich event 1 and the Younger Dryas. *Quaternary Science Reviews*, *107*, 129–137. https://doi.org/10.1016/j.quascirev.2014.10.021

McCave, I. N., & Andrews, J. T. (2019). Distinguishing current effects in sediments delivered to the ocean by ice. I. Principles, methods and examples. *Quaternary Science Reviews*, *212*, 92–107. https://doi.org/10.1016/j.quascirev.2019.03.031

McCave, I. N., & Hall, I. R. (2006). Size sorting in marine muds: Processes, pitfalls, and prospects for paleoflow-speed proxies. *Geochemistry, Geophysics, Geosystems*, *7*(10), 37. https://doi.org/10.1029/2006GC001284

McCave, I. N., Manighetti, B., & Robinson, S. G. (1995). Sortable silt and fine sediment size/composition slicing: Parameters for palaeocurrent speed and palaeoceanography. *Paleoceanography and Paleoclimatology*, *10*(3), 593–610. https://doi.org/10.1029/94PA03039

McCave, I. N., Thornalley, D. J. R., & Hall, I. R. (2017). Relation of sortable silt grain-size to deep-sea current speeds: Calibration of the 'Mud Current Meter'. *Deep Sea Research Part I: Oceanographic Research Papers*, *127*, 1–12. https://doi.org/10.1016/j.dsr.2017.07.003

Mirzaloo, M., Nürnberg, D., Kienast, M., & Lubbe, H. J. L. (2019). Synchronous changes in sediment transport and provenance at the Iceland-Faroe Ridge linked to millennial climate variability from 55 to 6 ka BP. *Geochemistry, Geophysics, Geosystems*, *20*(8), 4184–4201. https://doi.org/10.1029/2019GC008298

Mokeddem, Z., & McManus, J. F. (2017). Insights into North Atlantic deep water formation during the peak interglacial interval of Marine Isotope Stage 9 (MIS 9). *Climate Dynamics*, *49*(9–10), 3193–3208. https://doi.org/10.1007/s00382-016-3505-9

Mulder, T., Hassan, R., Ducassou, E., Zaragosi, S., Gonthier, E., Hanquiez, V., et al. (2013). Contourites in the Gulf of Cadiz: A cautionary note on potentially ambiguous indicators of bottom current velocity. *Geo-Marine Letters*, *33*(5), 357–367. https://doi.org/10.1007/s00367-013-0332-4

Paterson, G. A., & Heslop, D. (2015). New methods for unmixing sediment grain size data. *Geochemistry, Geophysics, Geosystems*, *16*(12), 4494–4506. https://doi.org/10.1002/2015GC006070

Richter, T. O., van der Gaast, S., Koster, B., Vaars, A., Gieles, R., de Stigter, H. C., et al. (2006). The Avaatech XRF core scanner: Technical description and applications to NE Atlantic sediments. *Geological Society, London, Special Publications*, *267*(1), 39–50. https://doi.org/10.1144/GSL.SP.2006.267.01.03

Seidel, M., & Hlawitschka, M. (2015). An R-Based function for modeling of end member compositions. *Mathematical Geosciences*, *47*(8), 995–1007. https://doi.org/10.1007/s11004-015-9609-7

Shimada, C., Sato, T., Toyoshima, S., Yamasaki, M., & Tanimura, Y. (2008). Paleoecological significance of laminated diatomaceous oozes during the middle-to-late Pleistocene, North Atlantic Ocean (IODP site U1304). *Marine Micropaleontology*, *69*(2), 139–150. https://doi.org/10.1016/j.marmicro.2008.07.004

Stevenard, N. (2023). IRD correction Matlab script [Software]. Zenodo. https://doi.org/10.5281/zenodo.7636179

Stevenard, N., Govin, A., Kissel, C., & Van Toer, A. (2023a). Geochemical ratio ln(Zr/Rb) from core MD03-2673 [Dataset]. PANGAEA. https://doi.org/10.1594/PANGAEA.950965

Stevenard, N., Govin, A., Kissel, C., & Van Toer, A. (2023b). Geochemical ratio ln(Zr/Rb) from core MD03-2679 [Dataset]. PANGAEA. https://doi.org/10.1594/PANGAEA.950967

Stevenard, N., Govin, A., Kissel, C., & Van Toer, A. (2023c). Sortable silt data from core MD03-2673 [Dataset]. PANGAEA. https://doi.org/10.1594/PANGAEA.950962

Stevenard, N., Govin, A., Kissel, C., & Van Toer, A. (2023d). Sortable silt data from core MD03-2679 [Dataset]. PANGAEA. https://doi.org/10.1594/PANGAEA.950966

Thornalley, D. J. R., Blaschek, M., Davies, F. J., Praetorius, S., Oppo, D. W., McManus, J. F., et al. (2013). Long-term variations in Iceland–Scotland overflow strength during the Holocene. *Climate of the Past*, *9*(5), 2073–2084. https://doi.org/10.5194/cp-9-2073-2013

Toucanne, S., Soulet, G., Riveiros, N. V., Boswell, S. M., Dennielou, B., Waelbroeck, C., et al. (2021). The North Atlantic Glacial Eastern Boundary Current as a key driver for ice-sheet—AMOC interactions and climate instability. *Paleoceanography and Paleoclimatology*, *36*(3), e2020PA004068. https://doi.org/10.1029/2020PA004068

Weltje, G. J. (1997). End-member modeling of compositional data: Numerical-statistical algorithms for solving the explicit mixing problem. *Mathematical Geology*, *29*(4), 503–549. https://doi.org/10.1007/BF02775085

Weltje, G. J., Bloemsma, M. R., Tjallingii, R., Heslop, D., Röhl, U., & Croudace, I. W. (2015). Prediction of geochemical composition from XRF core scanner data: A new multivariate approach including automatic selection of calibration samples and quantification of uncertainties. In I. W. Croudace & R. G. Rothwell (Eds.), *Micro-XRF studies of sediment cores* (pp. 507–534). Springer Netherlands. https://doi.org/10.1007/978-94-017-9849-5_21

Weltje, G. J., & Tjallingii, R. (2008). Calibration of XRF core scanners for quantitative geochemical logging of sediment cores: Theory and application. *Earth and Planetary Science Letters*, *274*(3–4), 423–438. https://doi.org/10.1016/j.epsl.2008.07.054

Wu, L. (2020). Dr. In G-cubed (1.1) [Dataset]. Zenodo. https://doi.org/10.5281/zenodo.4075009

Wu, L., Wang, R., Xiao, W., Krijgsman, W., Li, Q., Ge, S., & Ma, T. (2018). Late quaternary deep stratification-climate coupling in the Southern Ocean: Implications for changes in abyssal carbon storage. *Geochemistry, Geophysics, Geosystems*, *19*(2), 379–395. https://doi.org/10.1002/2017GC007250

Wu, L., Wilson, D. J., Wang, R., Yin, X., Chen, Z., Xiao, W., & Huang, M. (2020). Evaluating Zr/Rb ratio from XRF scanning as an indicator of grain-size variations of glaciomarine sediments in the Southern Ocean. *Geochemistry, Geophysics, Geosystems*, *21*(11), e2020GC009350. https://doi.org/10.1029/2020GC009350

Wu, S., Lembke-Jene, L., Lamy, F., Arz, H. W., Nowaczyk, N., Xiao, W., et al. (2021). Orbital- and millennial-scale Antarctic circumpolar current variability in Drake passage over the past 140,000 years. *Nature Communications*, *12*(1), 3948. https://doi.org/10.1038/s41467-021-24264-9

Xuan, C., Channell, J. E. T., & Hodell, D. A. (2016). Quaternary magnetic and oxygen isotope stratigraphy in diatom-rich sediments of the southern Gardar Drift (IODP Site U1304, North Atlantic). *Quaternary Science Reviews*, *142*, 74–89. https://doi.org/10.1016/j.quascirev.2016.04.010

Zhang, X., Wang, H., Xu, S., & Yang, Z. (2020). A basic end-member model algorithm for grain-size data of marine sediments. *Estuarine, Coastal and Shelf Science*, *236*, 106656. https://doi.org/10.1016/j.ecss.2020.106656

References From the Supporting Information

Poutiers, J., & Gonthier, E. (1978). Sur la susceptibilité magnétique des sédiments, indicateurs de la dispersion du matériel volcanoclastique à partir de l'Islande et des Faeroes. *Bulletin de l'Institut de Geologie du Bassin d'Aquitaine*, *23*, 214–226.